Cloud-tracked winds for the first Mars Global Surveyor mapping year

Huiqun Wang and Andrew P. Ingersoll

Division of Geological and Planetary Sciences, California Institute of Technology, Pasadena, California, USA

Received 22 April 2003; revised 11 June 2003; accepted 20 June 2003; published 30 September 2003.

[1] We have measured winds using cloud motion in consecutive Mars Global Surveyor (MGS) Mars Orbiter Camera (MOC) wide-angle global map swaths taken during the first mapping year (L_s 135°–360°–111°). We present a total of ~11,200 wind vectors collected in the north polar region during L_s 135°–195° (late summer/early fall) and L_s 20°–55° (mid spring) and in the south polar region during L_s 337°–10° (late summer/early fall). For cases with good coverage, we also present the derived mean zonal and meridional winds and the associated eddies. The speed of the zonal winds in 60°N–70°N increases at ~0.6 m/s/°L_s in late northern summer, and that in 60°S–70°S increases at a rate of ~0.7 m/s/°L_s in late southern summer. The latitudinal distribution of zonal wind within 50°N–75°N from mid northern summer to early northern fall indicates that winds at higher latitudes are generally weaker than those at lower latitudes, but the rate of increase with time is faster at higher latitudes. There is a cyclonic gyre in the 90°W–0°–30°E sector in the north polar region. There are large-scale waves in the weekly mean meridional wind and in the biweekly mean eddy momentum flux and eddy kinetic energy fields in the north polar region from mid to late summer. The cloud-tracked winds in the north are generally consistent with winds calculated by general circulation model at the water condensation level derived from MGS Thermal Emission Spectrometer (TES) observations but appear stronger than the gradient winds derived from TES assuming no flow at the surface. *INDEX TERMS:* 5409 Planetology: Solid Surface Planets: Atmospheres—structure and dynamics; 5462 Planetology: Solid Surface Planets: Polar regions; 5464 Planetology: Solid Surface Planets: Remote sensing; 5445 Planetology: Solid Surface Planets: Meteorology (3346); 6225 Planetology: Solar System Objects: Mars; *KEYWORDS:* Mars, winds, cloud tracking, Mars Global Surveyor, circulation, eddy

Citation: Wang, H., and A. P. Ingersoll, Cloud-tracked winds for the first Mars Global Surveyor mapping year, *J. Geophys. Res.*, *108*(E9), 5110, doi:10.1029/2003JE002107, 2003.

1. Introduction

[2] Wind measurements provide important constraints for general circulation models (GCMs). The two Viking landers recorded winds continuously at an altitude of 1.6 m [*Hess et al.*, 1977]. Pathfinder measured wind speeds at three heights within 1.2 m of the surface [*Sullivan et al.*, 2000]. However, these measurements are limited to only three locations. *Kahn* [1983] documented global wind directions derived from Mariner 9 and Viking data. However, wind speed has been deduced in only ~20 cases [e.g., *Kahn and Gierasch*, 1982; *Mischna et al.*, 1998]. In this paper, we report 11,219 wind vectors derived from cloud tracking for the first MGS mapping year.

[3] Mars Global Surveyor (MGS) is in a polar (2AM–2PM) orbit with a period of about two hours. The red (575–625 nm) and blue (400–450 nm) "push broom" wide-angle Mars Orbiter Cameras (MOC) on board MGS produce 7.5 km/pixel or 3.75 km/pixel global map swaths [*Malin and Edgett*, 2001]. Twelve consecutive swaths can cover the whole planet in one day. The large overlap of successive orbits in the polar regions provide an opportunity to gather wind measurements through cloud tracking.

[4] Winds can be measured from cloud motion when cloud features can be tracked in two or more images. For this study, we first process the raw global map swaths into polar stereographic images [*Wang and Ingersoll*, 2002]. We identify the same cloud feature in two images by eye, and draw a vector from the initial to the final position (Figure 1). We divide the distance between them by the time interval to get the velocity. We use two swaths separated by two hours. Most of our tracking is performed in areas where surface features register within 1 pixel between consecutive images. If we miss the true positions of the cloud features by four pixels, we will be ~30 km off in distance and ~4 m/s off in calculated velocity. Errors in the cloud-tracked winds can be reduced by tracking the same cloud feature in two frames separated by many orbits, but this depends on the lifetime of the recognizable features and the paths traveled by the cloud.

[5] The coverage of the wind measurements is far from uniform because the measurement depends on both the overlap area and the presence of clouds that are suitable for tracking. Due to the small overlap of the swaths in the equatorial region, we only track clouds in the north and

0148-0227/03/2003JE002107

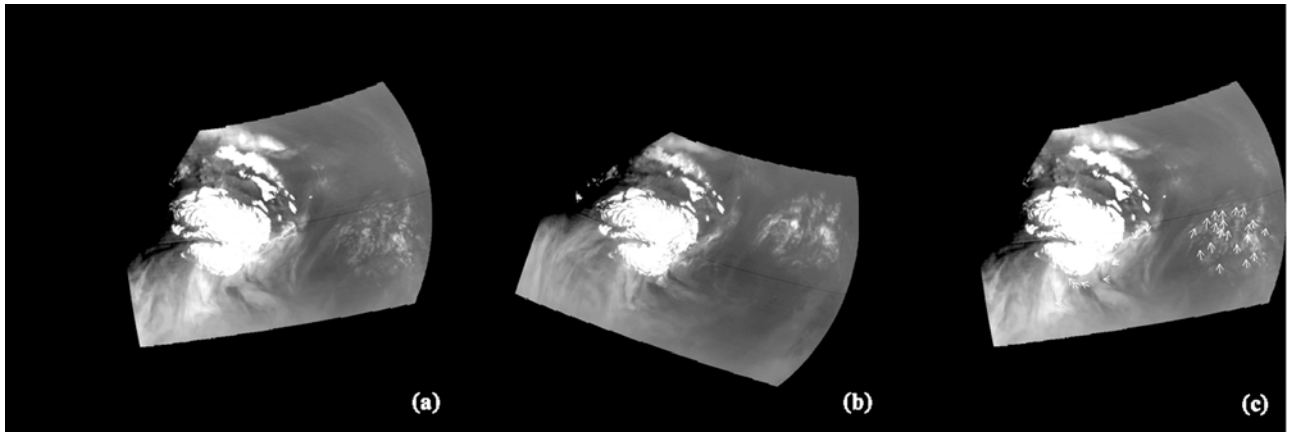

Figure 1. (a) (b) Consecutive projected MOC global map swaths (m01-01743 and m01-01756, 45°N–90°N) used for cloud tracking. (c) Measured wind vectors superimposed on the image in (a).

south polar regions (45°–90°N/S). There are generally more clouds in the north than in the south. Cloud amount sharply increases from mid summer to early fall, and greatly decreases from mid spring to early summer in both hemispheres [*Wang and Ingersoll*, 2002]. Stationary lee waves can only be used for wind direction. Haze is too diffuse for feature recognition. Streaks and fronts can be tracked in the perpendicular direction, but features are hard to identify along them. As a result, polar hood clouds that include haze, streaks, and lee waves are not good candidates for cloud tracking. Moreover, the large terminator circles in the polar stereographic mosaics during the fall and winter [*Wang and Ingersoll*, 2002] reduce the image overlap and useful data. These limitations confine the effective cloud tracking period in the first MGS mapping year (L_s 135°–360°–111°) to L_s 135°–195° and 20°–55° in the north polar region, and L_s 337°–10° in the south polar region.

[6] Uncertainty in cloud heights will limit the application of cloud-tracked winds, because both wind velocity and direction change with altitude. *Smith* [2002] derived the water vapor condensation level for the first MGS mapping year. His results show that during the three effective cloud tracking periods mentioned above, the cloud condensation level is ~10 km above the surface. However, the condensation level only indicates the cloud base of water ice clouds, and is not necessarily related to the height of the optically thick clouds used for tracking. The tracked clouds probably occurred at a variety of levels that spanned many kilometers. In order to derive circulation patterns from the collected wind vectors, we averaged weekly data in this paper and assumed that clouds observed on a weekly timescale formed under similar conditions and had similar cloud heights. In order to compare our measurements with GCM results, we used the NASA Ames GCM winds [*Haberle et al.*, 1993] at the condensation level derived by *Smith* [2002].

[7] We present cloud-tracked winds and the associated circulation patterns for each week in section 2. We derive zonal mean winds (zonal and meridional components) for each week in section 3. We analyze the latitudinal distribution of zonal winds in northern high latitudes during L_s 135°–195° in section 4. We show the Fourier wave components in meridional wind, and the eddy momentum flux and eddy kinetic energy maps for the north polar region in section 5. We summarize in section 6.

2. Cloud-Tracked Winds

2.1. North Polar Region During L_s 135°–195°

[8] Cloud-tracked winds for the north polar region (45°–90°N) during L_s 135°–195° are shown in Figure 2. Each panel contains results obtained from the 84 blue images taken during the period indicated below the panel (~1 week). A square dot in the panel represents the initial position of a cloud feature. A bar starts from the dot and ends at the final position of the same feature in the next image (~2 hours later). The total number of measurements (n) is indicated below each panel. It depends on the amount and type of cloud during the period, the overlap area of consecutive images, and the seasonal distribution of sunlight. The number of measurements generally increases from ~500/week before L_s ~160.5° to more than 800/week during L_s 160.5°–171.5°, then sharply decreases afterward.

[9] Winds south of 75°N generally blow eastward and increase in strength with time during L_s 135°–195°. Before L_s ~170°, winds north of ~75°N in the 90°W–0°–30°E sector blow westward. Cap edge winds in other sectors generally blow eastward. A number of vectors are collected over the polar cap during L_s 164°–171°, and generally point from the eastern to the western hemisphere (north at ~270°W, south at ~90°W).

[10] The circulation patterns resulting from the wind measurements can be seen from Figure 3. The lines in each panel start from the crosses and represent "averaged trajectories" of air parcels initially at the positions of the crosses. We first calculate the average wind speed within a radius (typically 250 km, ~4.2° of latitude) of an initial position represented by a cross, and integrate forward to the next position (the time step varies with the mean velocity, and is typically minutes). We then take this new position as the starting point and integrate one more step. This process is repeated until no further integration is possible due to lack of measurements. A line is formed by sequentially connecting the resulting positions. Each cross represents a starting point of such an integration process. The lines only represent wind direction. Closely spaced lines mainly reflect that

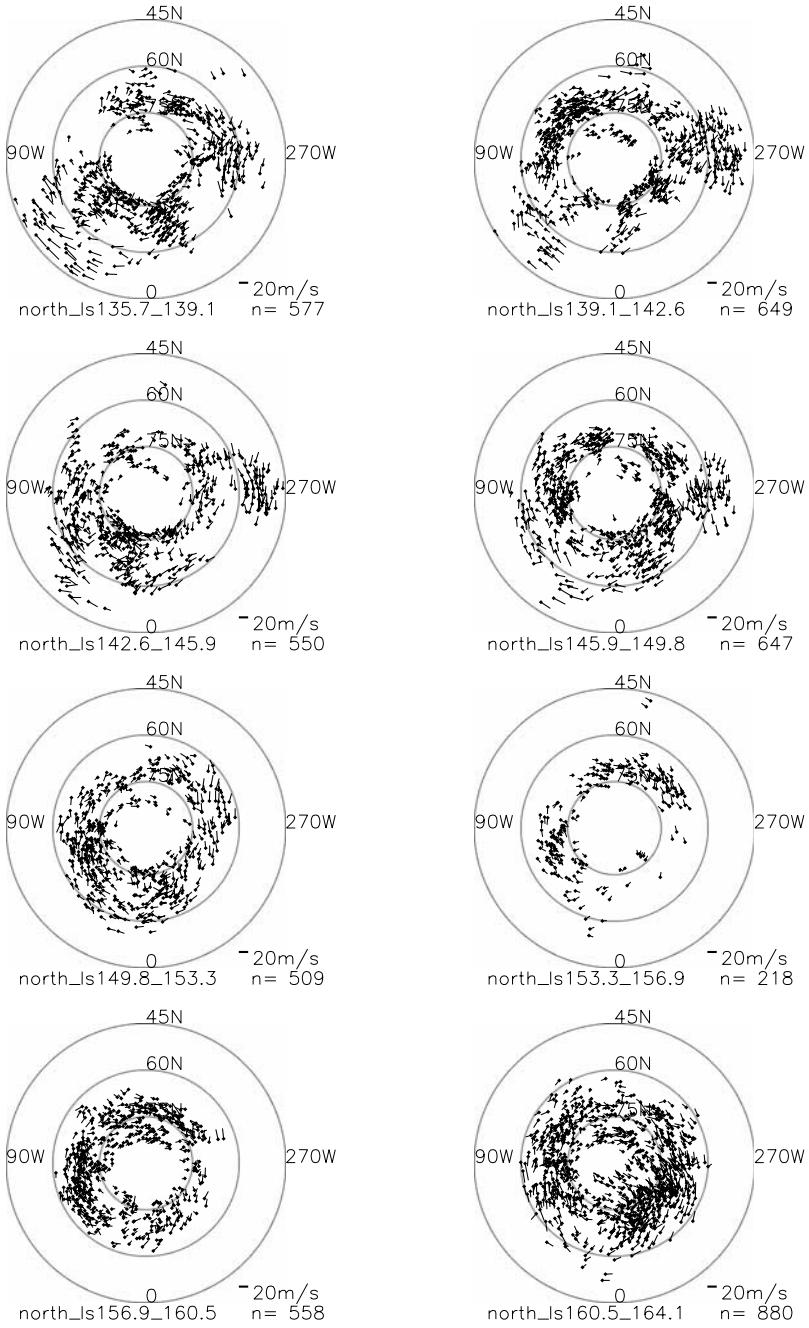

Figure 2. Wind vectors collected for the north polar region from mid northern summer to early northern fall. The Ls, total number of vectors, and scale bar are indicated below each panel. The circles represent 45°N, 60°N, and 75°N respectively. Longitudes and latitudes are indicated in each panel.

many measurements are collected in the neighborhood. The spacing between the lines is not inversely proportional to wind velocity, as would be the case if the lines were streamlines. Figure 3 shows the changing north polar vortex on a weekly timescale. The vortices deviate from the latitudinal circles, and are usually elongated along an axis (which changes with time).

[11] Before L_s ~170°, there is a cyclonic gyre in the 90°W–0°–30°E sector. It results from the westward wind at the cap edge in this sector and the eastward winds further south. This area lies north of Acidalia Planitia, and corresponds to the strongest "storm zone" simulated by the NASA Ames GCM [*Hollingsworth et al.*, 1996]. Many frontal clouds have been observed in this sector [*Wang and Ingersoll*, 2002], indicating that the special circulation pattern may be favorable for baroclinic storm development.

2.2. North Polar Region During L_s 20°–55°

[12] Cloud-tracked winds for the north polar region during L_s 20°–55° are shown in Figure 4, and the derived air parcel trajectories for selected weeks are shown in Figure 5. The number of vectors gathered each week during this period is much less than that during L_s 160.5°–171.5°, reflecting the decreased number of clouds suitable for tracking. The

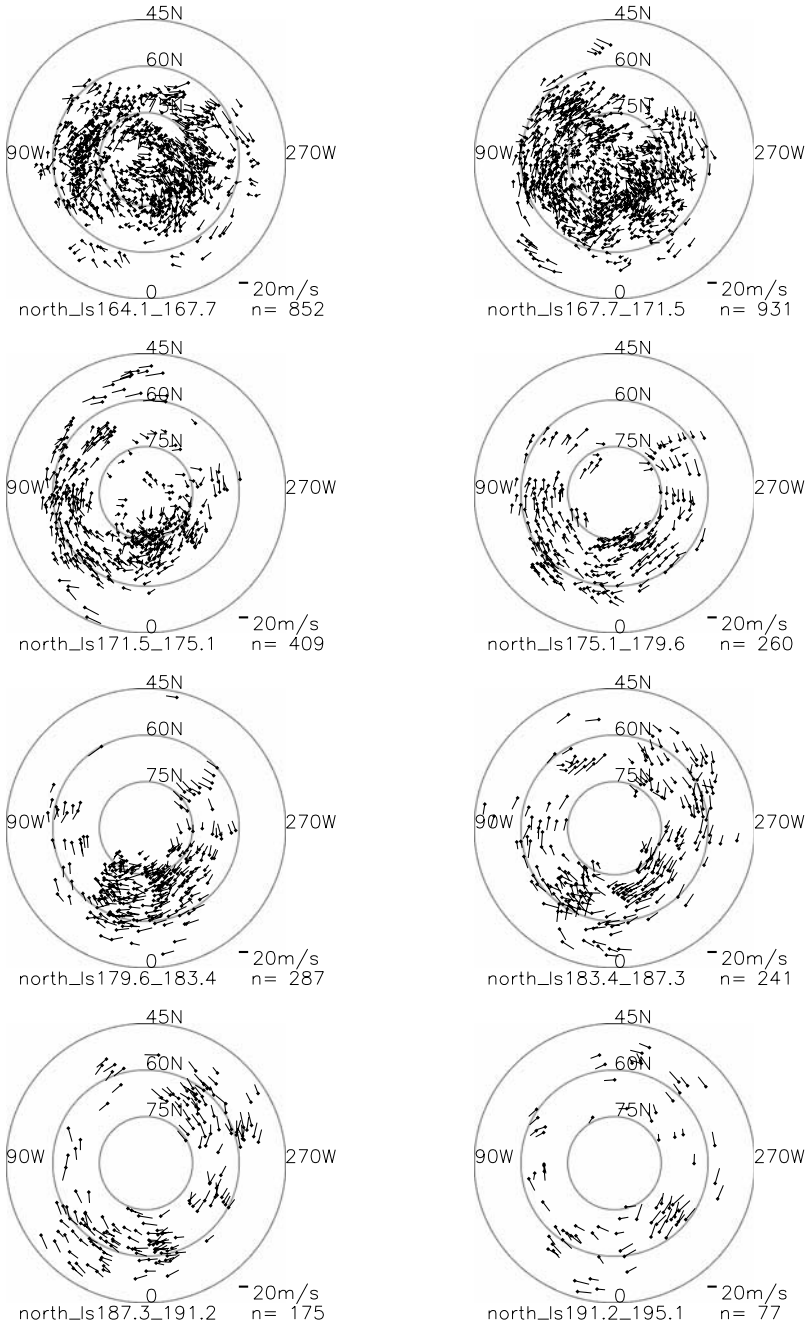

Figure 2. (continued)

number of measurements quickly decreases from ~300/week before L_s ~36° to ~150/week afterward. Winds south of ~75°N generally blow eastward and weaken with time. A cyclonic gyre in the 0°–90°W sector is derived for the week of L_s 27.2°–30.4°. Vectors over the polar cap generally point from the eastern to western hemisphere (north at ~270°W, south at ~90°W) before L_s ~52°. However, they change to the opposite direction afterward, suggesting a circulation transition from spring to summer.

2.3. South Polar Region During L_s 337°–10°

[13] Cloud-tracked winds for the south polar region (45°–90°S) during L_s 337°–10° are shown in Figure 6. Since most of the good candidates for cloud tracking in the south are dust clouds that appear most clearly through the red filter, each panel here contains measurements from 84 red images taken during a week. Note that dust clouds may be at a different altitude than water ice clouds. The number of measurements is much fewer than that in the north polar region, reflecting the relative lack of clouds and water vapor in the southern hemisphere. Winds north of 75°S generally blow eastward and increase in strength from southern summer to fall. Southwestward winds are sometimes observed south of 75°S, especially in the 180°W–270°W sector. Circulation patterns are not shown for these measurements because of the poor spatial coverage.

[14] Sparse measurements are also collected for the south polar region in mid (L_s 216°–238°) and late southern spring

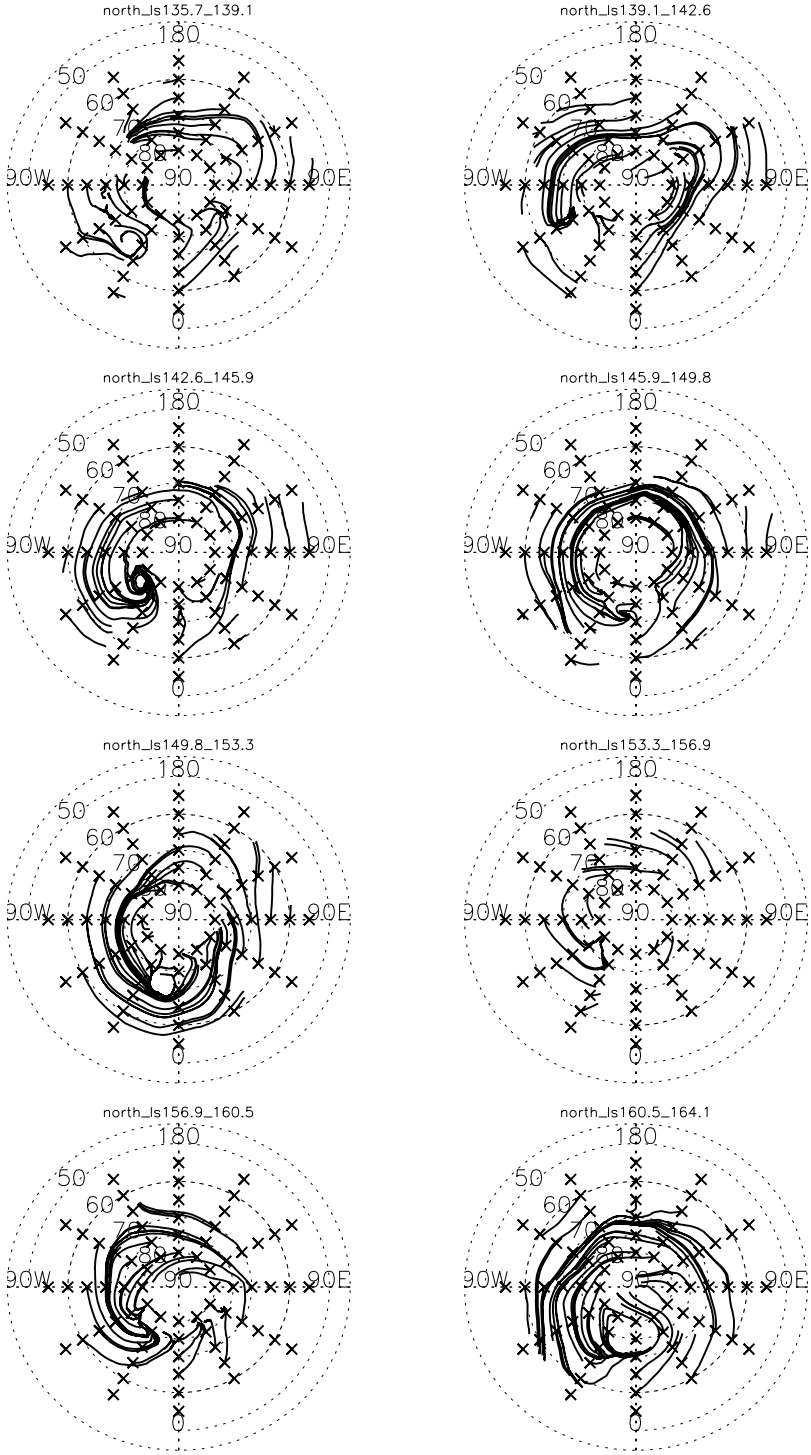

Figure 3. Circulation patterns derived for each panel in Figure 2. See section 2.1 for details. Longitudes and latitudes are indicated in each panel.

(L_s 254°–262°) (not shown). Results show that during mid spring, there are eastward winds (10–15 m/s) north of 75°S. As summer approaches, the number of dust storms in the south polar maps decrease greatly, and the only tractable features are the arc-shaped cap edge clouds near the terminator [*Wang and Ingersoll*, 2002]. The motion of these clouds shows off-cap winds in the early evening before southern summer solstice. Our results are roughly consistent with the Viking and Mariner 9 wind directions derived by *Kahn* [1983].

3. Zonal Mean Winds

[15] Figure 7 shows the mean zonal ($\bar{u}$) and meridional ($\bar{v}$) winds for 60°–70°N/S and 70°–80°N/S as a function of L_s for the three cloud tracking periods presented above. Each

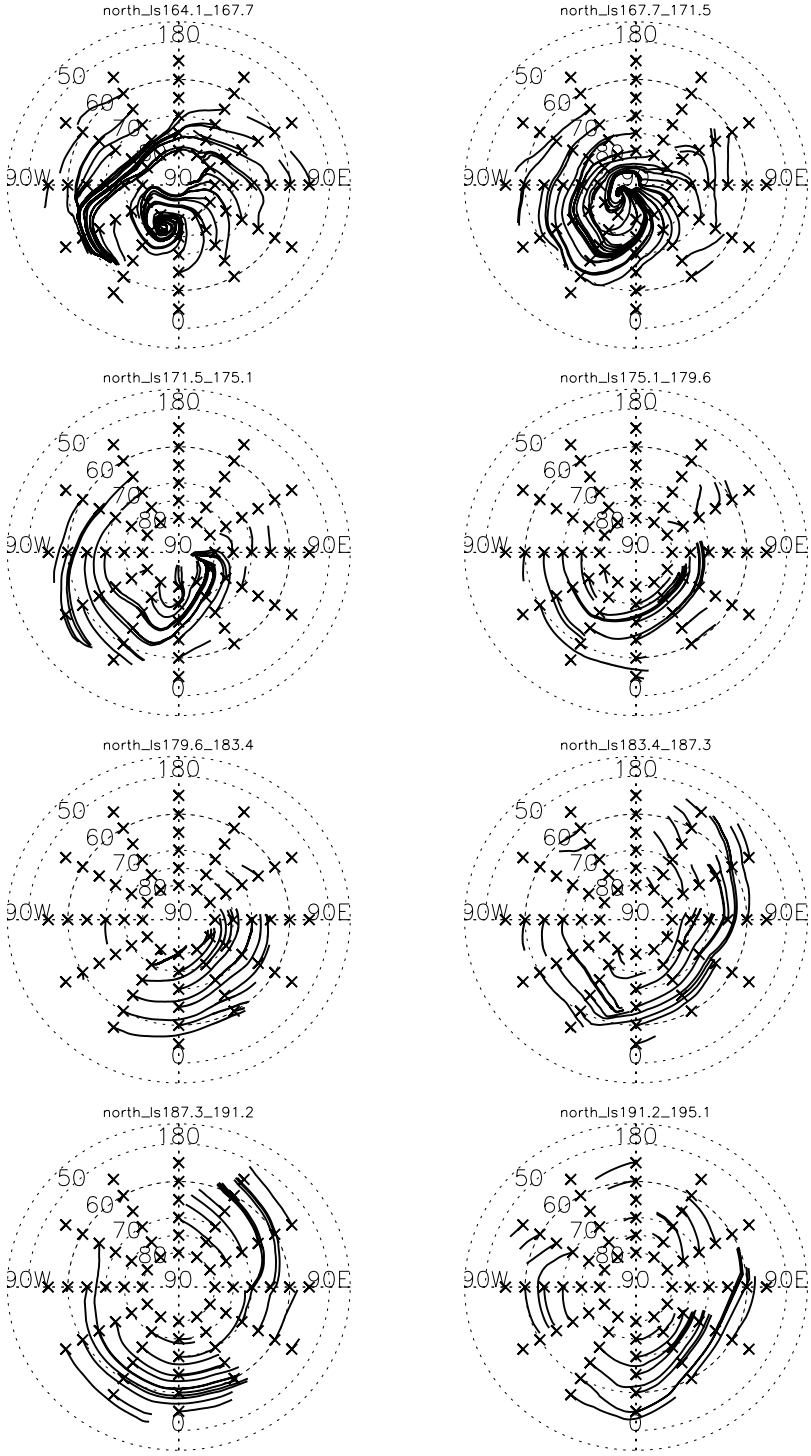

Figure 3. (continued)

data point is derived from a panel in Figure 2, 4, or 6. $L_s >$ 360° represents the next Martian year. The error bars represent standard deviation of the mean, i.e., $\sigma/\sqrt{n}$, where σ^2 is the variance, $\sigma^2 = \sum(x-\bar{x})^2/(n-1)$, x represents u or v (u > 0 for eastward wind, v > 0 for northward wind), $\bar{x}$ is the mean of x, and n is the total number of measurements within the latitudinal bin. Cases with n < 20 are neglected. σ is typically ∼5m/s. The small error bars for the period L_s 135°–195° reflect the large number of vectors gathered for each week. Since the longitudinal distribution of measurements are nonuniform, the calculated $\bar{u}$ and $\bar{v}$ are biased toward the velocity of the areas with dense coverage. For example, if most of the measurements are concentrated within areas where winds are weak, then the calculated $\bar{u}$ and $\bar{v}$ will be smaller then their true values. This bias is expected to be small for most of the cases in Figure 7, but data such as those for 60°N–70°N during L_s 40°–55° and many south polar results should be used with caution. We

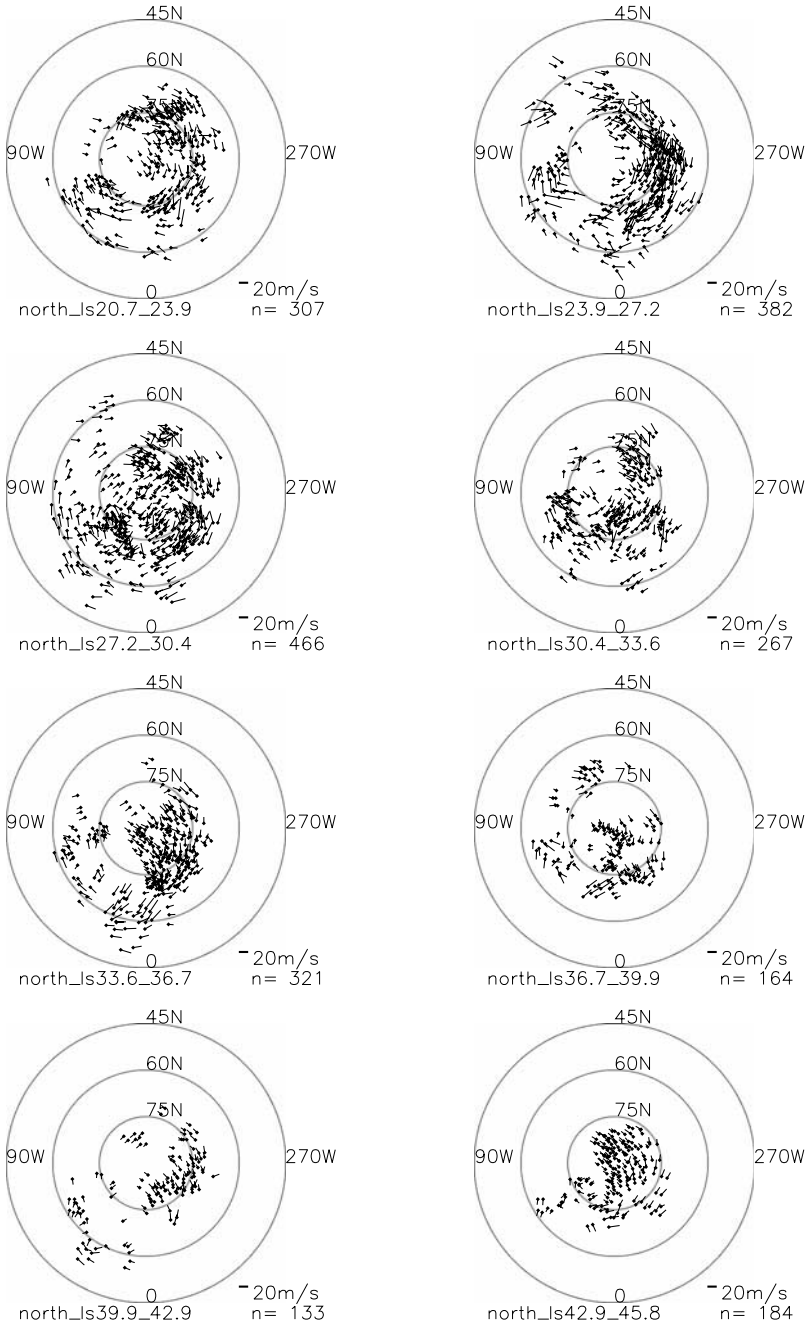

Figure 4. Wind vectors collected in the north polar region during northern spring. The L_s, total number of vectors, and scale bar are indicated below each panel. Longitudes and latitudes are indicated in each panel.

will assume that $\bar{u}$ and $\bar{v}$ represent the true values in the following discussion.

3.1. North Polar Region During L_s 135°–195°

[16] The zonal wind ($\bar{u}$) in 60°N–70°N fluctuates within 10–13 m/s during L_s 135°–166°, then smoothly increases at ~0.6 m/s/°L_s to ~23 m/s by L_s ~185° (Figure 7a). *Haberle et al.* [1993] presented latitude-altitude cross sections of zonal wind simulated by the NASA Ames GCM. Their Figure 12 shows that during L_s 140°–166°, $\bar{u}$ in 60°N–70°N increases with height and decreases with latitude. In the simulations, the altitude range where the winds are 10–13 m/s is 4–8 km at 60°N and 8–11 km at 70°N, suggesting a height of 7.5 ± 3.5 km for our cloud-tracked winds during a similar period. Many cloud-tracked winds are subject to local or regional circulations that could not be represented by GCM. Nonetheless, the height range above is consistent with the <10 km condensation level near the cap edge during this period [*Smith*, 2002]. *Smith et al.* [2001] derived gradient winds (balancing pressure gradient force, Coriolis force, and centrifugal force) from atmospheric temperatures retrieved from MGS TES, assuming zero

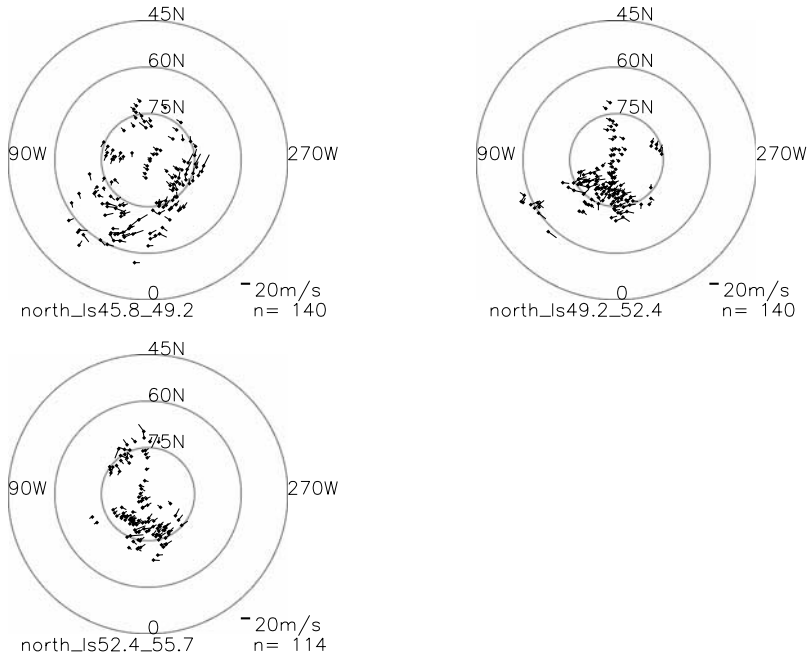

Figure 4. (continued)

winds at 7.1 mb. Their results for L_s = 135° show that the winds are less than 10 m/s below 10 km, which is the condensation level derived by *Smith* [2002]. This speed is less than the 10–13 m/s speeds that we measure, indicating that one of the assumptions, e.g., zero winds at the surface or measured winds below 10 km altitude, is wrong. For comparison, the gradient wind calculation gives winds of 10–13 m/s at altitudes of 12–14 km, which is above the condensation level according to *Smith* [2002]. It should be noted, however, TES retrievals are uncertain in the lower atmosphere [*Smith et al.*, 2001], and errors in the derived wind field are probably significant.

[17] The rapid increase of $\bar{u}$ during L_s 166°–185° is expected from the increasing latitudinal temperature gradient and is consistent with GCM simulations and TES data [*Haberle et al.*, 1993; *Smith et al.*, 2001]. The increasing trend in wind velocity could also be related to systematic increase in cloud height. The water vapor condensation level near the north polar cap sharply increases from <10 km to >40 km in early northern fall [*Smith*, 2002], indicating increasing height of water ice clouds with time. Since zonal winds increase with both height and L_s, larger values of $\bar{u}$ after L_s ~185° are expected from cloud tracking. However, the observed $\bar{u}$ levels off at ~23 m/s. Many vectors in early northern fall are derived from streak clouds which are the most representative features in the polar hood [*Wang and Ingersoll*, 2002]. Since we only track the wind component that is perpendicular to the streak clouds, the true wind velocity could be larger.

[18] Zonal wind in 70°N–80°N follows a similar trend as that in 60°N–70°N. However, the velocity is generally smaller and the rapid strengthening of wind occurs ~7° L_s later (Figure 7b). The water vapor condensation level in this latitudinal band is lower than that in 60°N–70°N, indicating lower water ice clouds. Zonal wind cross section simulated by NASA Ames GCM for L_s 140°–166° [*Haberle et al.*, 1993] show that the northern hemisphere zonal jet in the height range of 5–10 km peaks around 55°N with decreasing wind strength toward the north pole and equator. Since $\bar{u}$ increases with height at fixed latitude and decreases with latitude at fixed height, the factors mentioned above would contribute to weaker zonal wind in 70°–80°N than that in 60°–70°N. The timing of the rapid strengthening of winds can be affected by changes in both the wind field structure and the cloud height.

[19] The meridional wind ($\bar{v}$) in 60°N–70°N is on average +1.2 m/s during L_s 135°–166°, ~0 during L_s 166°–185°, and −1.8 m/s during L_s 185°–195° (Figure 7a). $\bar{v}$ in 70°N–80°N remains at 0 during L_s 135°–160°, +3 m/s during L_s 165°–180°, −1.7 m/s afterward. Negative $\bar{v}$ (southward) is derived only for cases with poor longitudinal coverage. Large meridional winds are associated with the cyclonic gyres in the circulation (Figures 2 and 3). On-cap winds in the eastern part of the gyre generally have higher velocity than off-cap winds in the western part of the gyre, resulting in average northward flow. Column water vapor abundance derived from TES decreases with latitude in northern mid and high latitudes during L_s 150°–195° [*Smith*, 2002]. If the same latitudinal trend holds at the height of our measurements, then our data suggest poleward transport of water vapor by the gyre at least during L_s 150°–180°. In contrast to our observations, the GCM simulated $\bar{v}$ in 60°N–70°N for L_s 140°–160° is southward at the levels where water ice clouds are expected (5–10 km) [*Haberle et al.*, 1993]. However, since the spatial coverage of our measurements is nonuniform, the derived mean meridional wind is probably biased, and the direction of water vapor transport by the polar circulation remains unclear.

3.2. North Polar Region During L_s 25°–55°

[20] The zonal wind ($\bar{u}$) in 60°N–70°N quickly decreases from ~20 m/s to ~10 m/s during L_s 25°–35°, and then

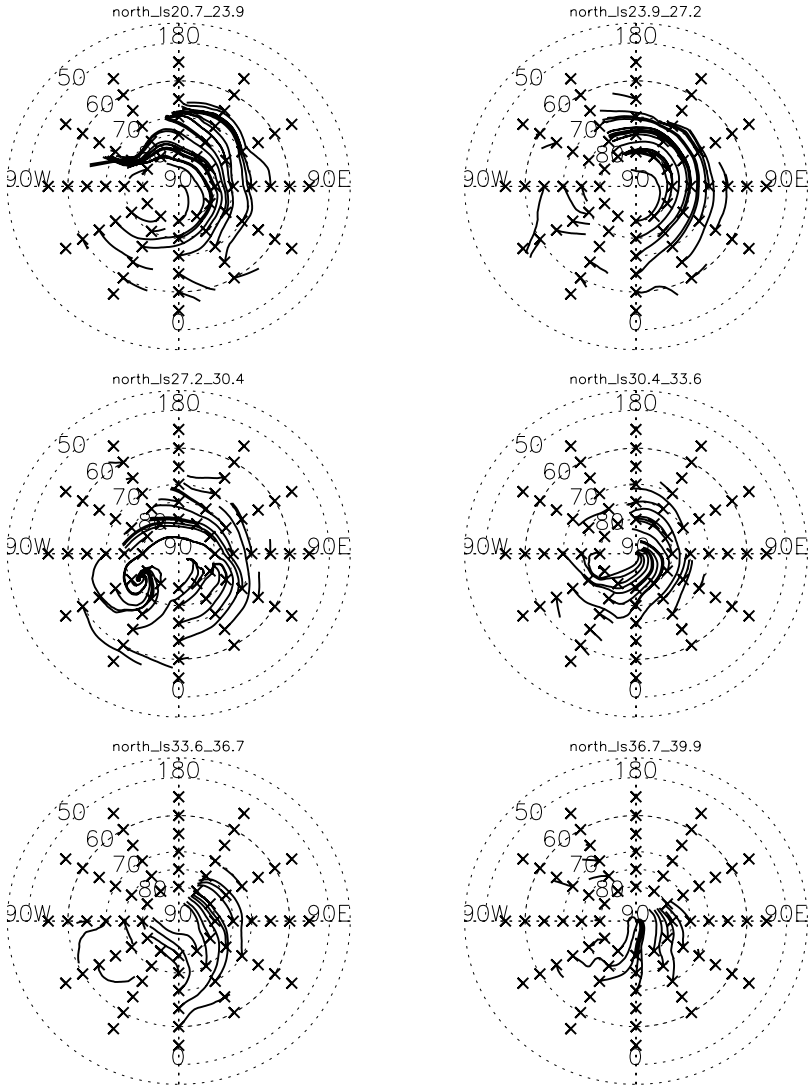

Figure 5. Circulation patterns derived for selected panels of Figure 4. See section 2.1 for details. Longitudes and latitudes are indicated in each panel.

fluctuates around 10 m/s in mid northern spring (Figure 7c). *Haberle et al.* [1993] simulated 20 m/s zonal wind in 60°N–70°N at ~8 km for L_s 0°–23°. This height is consistent with the <10 km water vapor condensation level near the north polar cap in early northern spring [*Smith*, 2002]. The condensation level gradually increases to 10–12 km in mid spring, indicating higher water ice clouds and thus stronger winds [*Smith*, 2002]. This effect must be counteracted by the decreasing latitudinal temperature gradient which decreases the zonal wind.

[21] A similar trend is observed for $\bar{u}$ in 70°N–80°N, but the velocities are smaller and the decreasing trend lasts until L_s ~38° (Figure 7d). The meridional wind ($\bar{v}$) in 70°N–80°N is positive (northward) during L_s 20°–55°, and can reach +5 m/s during L_s 35°–42° (Figure 7d). *Haberle et al.* [1993] simulated northward wind in 70°N–80°N within the 5–10 km altitude range for L_s 0°–23°. The meridional wind ($\bar{v}$) in 60°N–70°N is generally positive with exceptions during L_s 40°–45°. Examining Figure 4, we find that measurements after L_s ~40° are much sparser, and are concentrated within certain longitudinal sectors especially south of 75°N.

3.3. South Polar Region During L_s 337°–10°

[22] The zonal winds in 60°S–70°S increase from ~10 m/s to 19 m/s during L_s 355°–8° (Figure 7e). This increase with L_s (~0.7 m/s/°L_s) is a little faster than the 0.6 m/s/°L_s for $\bar{u}$ in 60°N–70°N during L_s 166°–185°. The zonal winds in 70°S–80°S generally increase with L_s as well (Figure 7f). (The data for L_s 337.8°–341.8° are probably biased due to the poor coverage (see Figure 6)). The latitude–height cross section of zonal wind for L_s 0°–23° simulated by NASA Ames GCM shows that 10–15 m/s winds occur within ~3 km of the surface at southern high latitudes [*Haberle et al.*, 1993]. In comparison, the water vapor condensation level is 5–10 km [*Smith*, 2002]. Since most clouds we tracked for the south polar region are dust clouds in red images, the discrepancy between the cloud height indicated by the NASA Ames GCM and that indicated by the water condensation level can be explained if the dust clouds are near the surface.

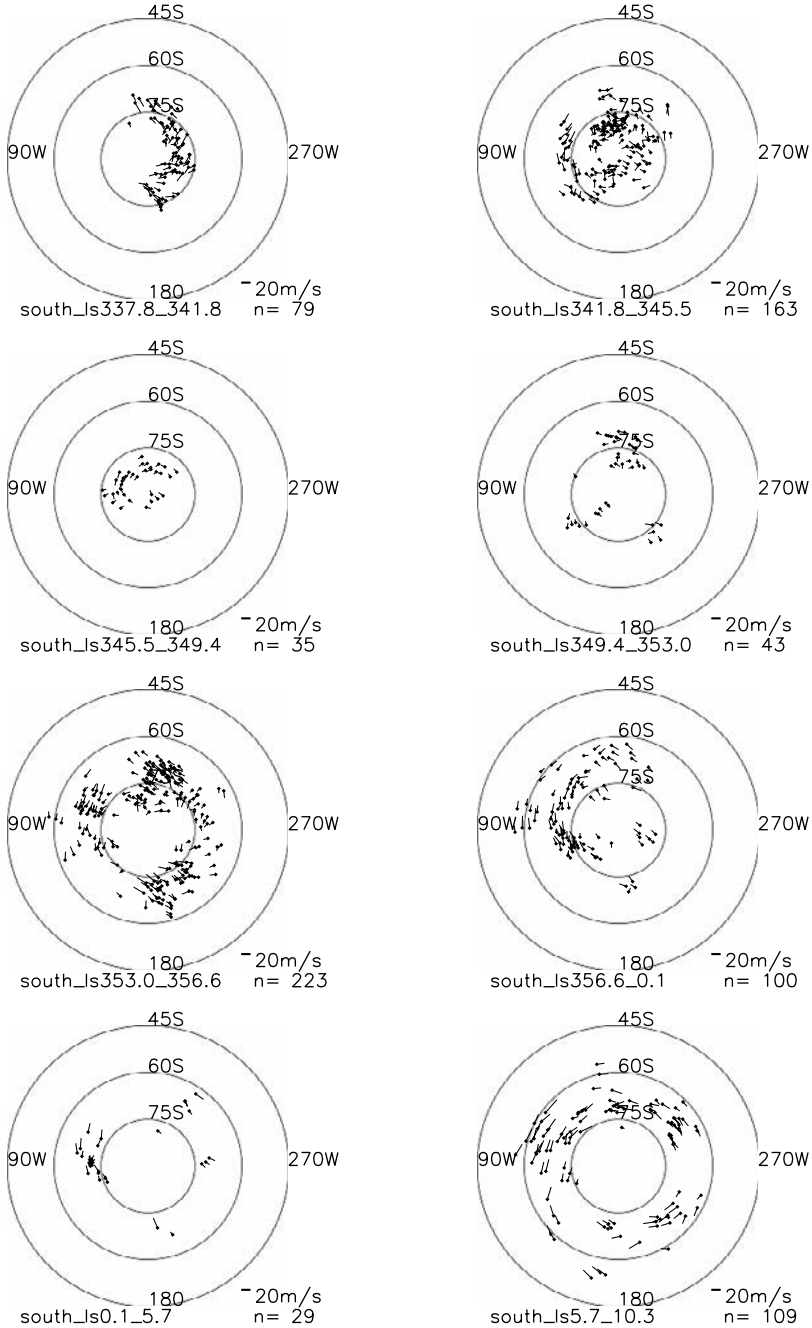

Figure 6. Wind vectors collected in the south polar region from mid summer to early fall. Longitudes and latitudes are indicated in each panel.

The meridional wind in southern high latitudes are southward (poleward) during L_s 340°–10°. This agrees with the lower branch of a meridional circulation cell with air rising near the pole and sinking in mid latitudes as the NASA Ames GCM has simulated for L_s 0°–23° [*Haberle et al.*, 1993].

4. Latitudinal Distribution of Zonal Wind

[23] The latitudinal distribution of zonal wind ($\bar{u}$) in 50°N–75°N for four consecutive 4-week periods during L_s 135.7°–195.1° is shown in Figure 8a. Each data point in Figure 8a is calculated by averaging all measured zonal winds within 2.5° of the central latitude. Cases when the number of measurements is less than 60 are neglected. The error bar represents the standard deviation of the mean which is defined in the previous section. To investigate to what degree the data can be explained by solid body rotation, we calculated $\bar{u}/\cos$ (latitude) for each latitudinal bin. The results for each week are shown in Figure 8b. Pure solid body rotation will result in a horizontal line, with larger values corresponding to faster rotation. To investigate the possibility of inertial instability and barotropic instability, we plotted the absolute vorticity of the mean flow ($Q = f - d\bar{u}/dy$) in Figure 8c for each period, where y is the distance between the latitudinal intervals, and f

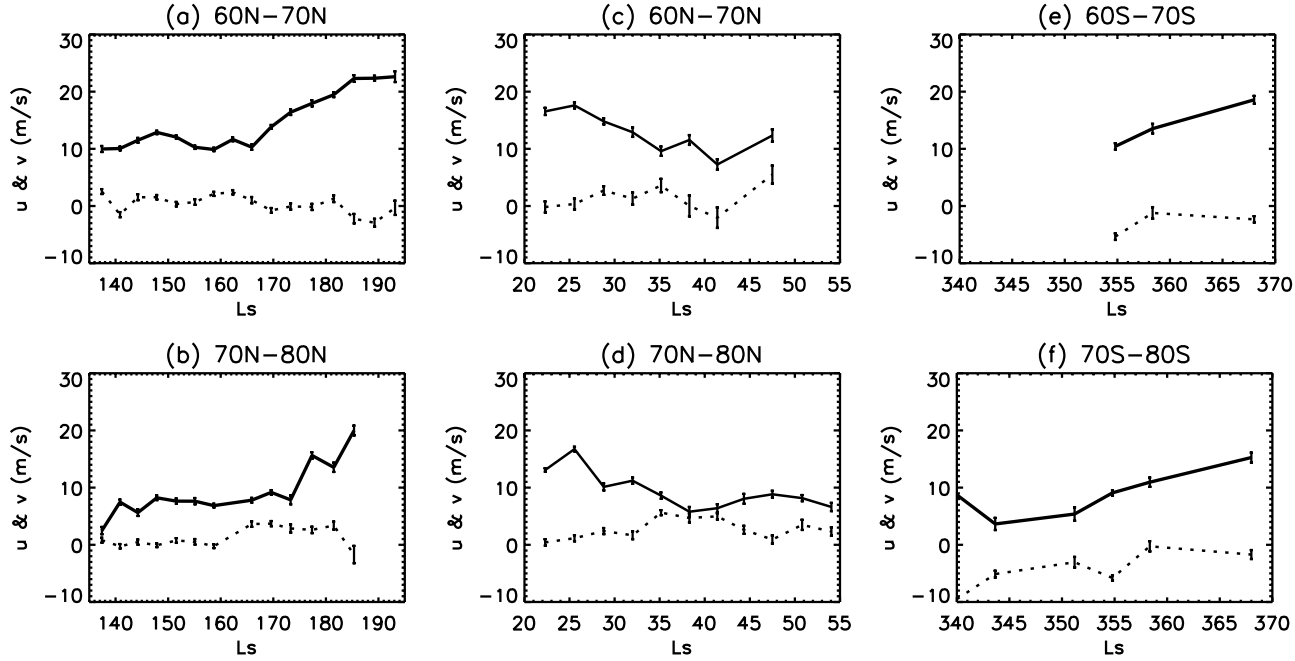

Figure 7. Zonal mean zonal ($\bar{u}$, m/s, solid line) and meridional ($\bar{v}$, m/s, dotted line) winds in 60°−70°N/S and 70°−80°N/S derived from Figures 2, 4, and 6. The error bars represent the standard deviation of the mean. See section 3 for detail.

is the Coriolis parameter. Zonal flow is inertially stable if the absolute vorticity is positive [*Salby*, 1996]. A necessary condition for barotropic instability is that dQ/dy changes sign somewhere in the interior [*Salby*, 1996]. To investigate if the winds were results of an angular momentum conserving Hadley circulation, we plotted angular momentum for each latitudinal band and time period in Figure 8d. We have assumed that all the measurements were at the same height in this section.

[24] Figure 8a shows that $\bar{u}$ generally decreases with latitude at least before $L_s \sim 180°$, indicating that the data are located on the poleward side of the jet stream. Figure 8a also shows that $\bar{u}$ for each latitudinal bin increases with L_s from mid northern summer to early northern fall. The increase becomes faster with time. Moreover, the increase at higher latitudes is larger than that at lower latitudes, resulting in a shallower slope of $d\bar{u}/dy$ at later times. The mean slopes for the four consecutive periods are −0.52, −0.46, −0.44, and −0.33 m/s/°latitude respectively. Difference in zonal wind structure could lead to different eddy activities and eddy-mean flow interactions [*Barnes et al.*, 1993].

[25] Most data before $L_s \sim 180°$ are roughly consistent with solid body rotation (Figure 8b), with an apparent increase in angular velocity during L_s 150°−180°. The exceptionally low value at 74°N for L_s 135.7°−149.8° results from the westward (negative) winds near the polar cap in the 90°W−0°−30°E sector (see Figures 2 and 3). The rate of rotation greatly increases during L_s 180°−195° at all latitudes where data exist. The increase is larger at higher latitudes, leading to the deviation from solid body rotation in Figure 8b.

[26] All the derived absolute vorticities in Figure 8c are positive, indicating inertially stable zonal flows. The latitudinal slope of dQ/dy changes from positive to negative to positive with increasing latitude during L_s 135.7°−149.8° and L_s 179.6°−195.1°. It changes from positive to negative during L_s 164.1°−179.6°, and from negative to positive during L_s 149.8°−164.1°. In summary, dQ/dy changes sign somewhere in 60°N−70°N during L_s 135°−195°, suggesting possible barotropic instabilities in this region. If the curvature of the vertical profile of $\bar{u}$ is large, vertical shear can become the dominant factor in potential vorticity (P), and change the sign of the slope of dP/dy (where $\frac{dP}{dy} = \frac{dQ}{dy} - \frac{1}{\rho}\frac{\partial}{\partial z}\left(\frac{f^2}{N^2}\rho\frac{\partial \bar{u}}{\partial z}\right)$, ρ is atmospheric density, N^2 is Brunt−Vaisailla frequency), signaling possible baroclinic instability [*Salby*, 1996].

[27] The angular momentum ($M = (\bar{u} + \Omega\, a \cos\theta) \cdot a \cos\theta$) deceases toward the pole in 50°N−75°N (Figure 8d) for all four periods. The planet rotation term ($\Omega\, a \cos\theta$) is greater than ∼65 m/s within 50°N−75°N. It is substantially larger than the measured $\bar{u}$ (< 25 m/s) in the latitudinal range. So, the latitudinal trend of M in Figure 8d is mainly determined by the rotation of Mars. The angular momentum for L_s 179.6°−195.1° is larger than that for other periods due to the greater $\bar{u}$. In the ideal case of zero stresses, Hadley circulation conserves angular momentum. Near the zonal westerly jet, strong barotropic and baroclinic instabilities lead to large eddy stresses, angular momentum converges in the disturbed region [*Held*, 2001]. Our results suggest that the measured winds are not parts of an angular momentum conserving Hadley circulation. This is also consistent with the winds being on the poleward side of the zonal jet which lie at the northern edge of the Hadley cell.

5. Eddy Winds

5.1. Fourier Wave Components

[28] On the basis of the data coverage, we analyze the Fourier wave components at 70°N during L_s 135°−172°. We choose 48 uniformly distributed grid points (∼150 km

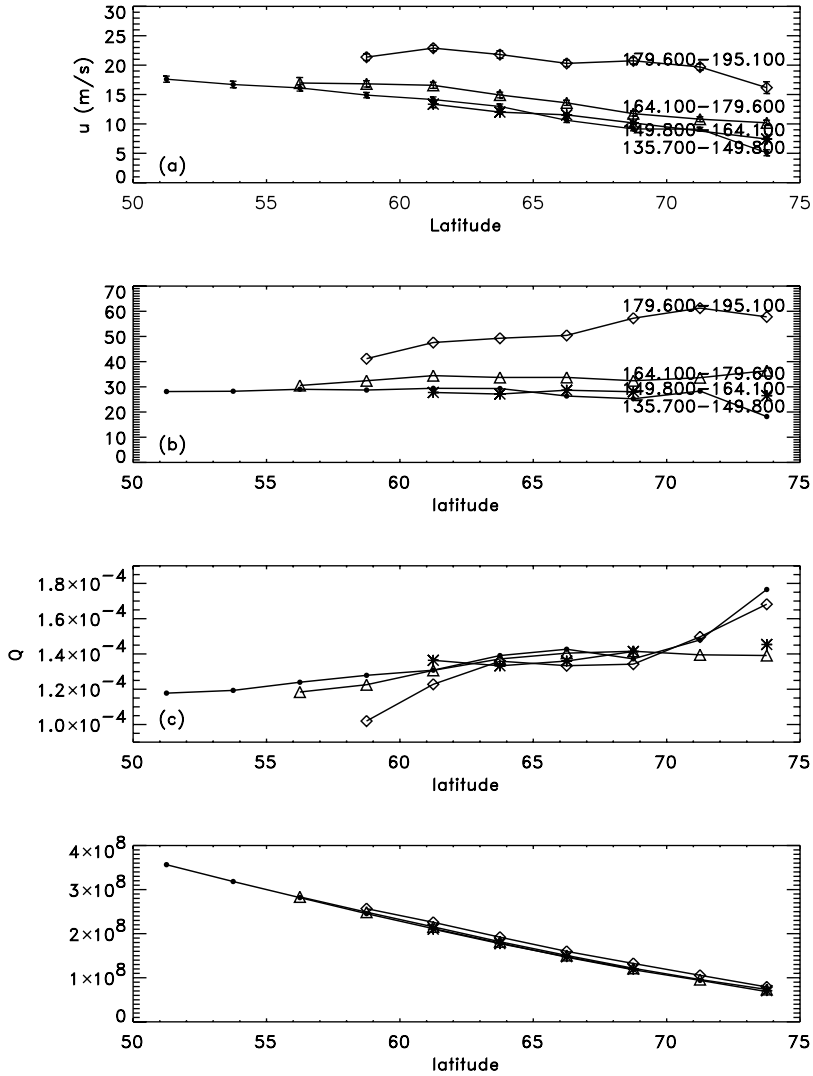

Figure 8. (a) Latitudinal distribution of zonal winds ($\bar{u}$ m/s) within 50°N–75°N for L_s 135.7°–149.8° (dot), L_s 149.8°–164.1° (star), L_s 164.1°–179.6° (triangle), and L_s 179.6°–195.1° (diamond). (b) Latitudinal distribution of $\bar{u}$/cos(latitude) for each curve in (a). (c) Latitudinal distribution of absolute vorticity $Q = f - d\bar{u}/dy$ for each curve in (a). (d) Latitudinal distribution of angular momentum $M(\mathrm{m}^2/\mathrm{s}^2)$ for each curve in (a).

spacing) along the 70°N latitudinal circle, and calculate the local average meridional wind v* by averaging the measurements within 300 km of each grid point for each week. If the number of measurements near a grid point is less than 6, then v* is labeled missing. If the total number of missing points along the latitudinal circle is less than 12, then linear interpolation is performed to fill in the missing data. The results are displayed as dots in Figure 9a. The dashed lines denote 0 m/s for the week. The interval between the tick marks on the vertical axis is 5 m/s. The over plotted solid lines in Figure 9a are composed from Fourier components up to wave 3. The general longitudinal variations are well represented by the first three waves. The longitude-L_s cross sections for Wave 1, 2, and 3 are shown in Figure 9b, 9c, and 9d respectively (with the same shading scheme as the bar next to the Wave 1 panel).

[29] Before L_s ~160°, Wave 1 has a mean amplitude of ~±2 m/s, with northward v* at ~335°W and southward v* at ~155°W. After L_s ~160°, the amplitude of Wave 1 is in the range of 4–8 m/s, and the northward and southward v* rotate eastward to ~265°W and ~85°W respectively. Referring to Figure 3, we see that larger amplitude Wave 1 is related to the polar vortex whose center is farther away from the pole. The amplitudes of Wave 2 range from ±1 to ±5 m/s during L_s 135°–172°, and those of Wave 3 range from ±1 to ±3 m/s. Referring to Figure 3, we see that large amplitude Wave 2 during L_s 139.1°–142.6° and 149.8°–153.3° corresponds to elliptical trajectories. Northward v* for Wave 2 is usually found at ~170°W and ~350°W. Northward v* for Wave 3 is usually found at ~90°W, 210°W, and 330°W. Both the amplitude and phase of Wave 2 and 3 appear to oscillate with time, with the oscillation period of amplitude being approximately half of the period of phase. Figures 9c and 9d indicate that the phase of Wave 2 oscillates with a period of ~10 weeks and an amplitude of ~25° in longitude, while the phase of Wave 3 oscillates

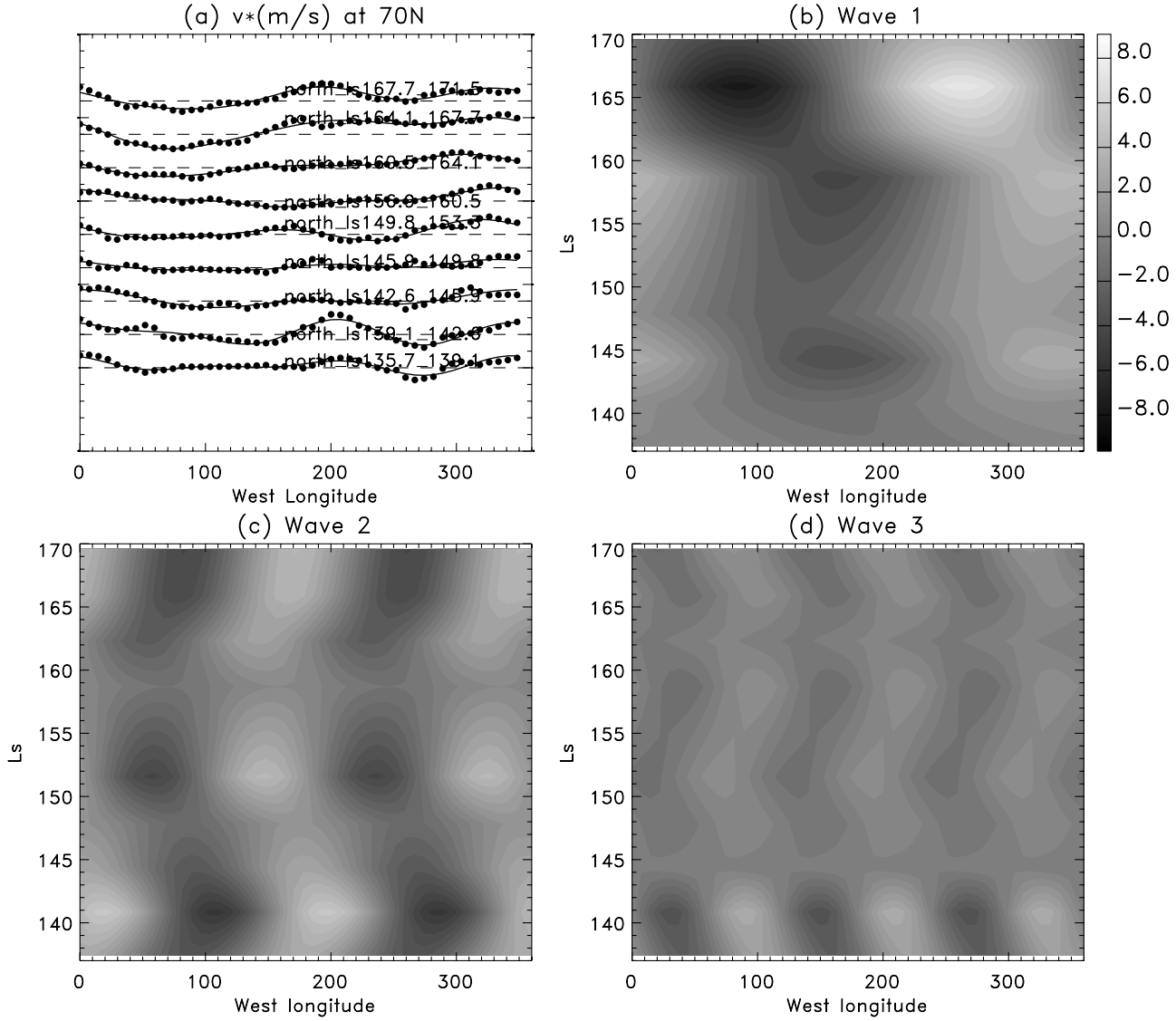

Figure 9. (a) Meridional winds (v*, m/s, dots) at 70°N. The curves are derived from Fourier components up to Wave 3. The dashed lines represent 0 m/s for each set of data. The Ls for each period is indicated in the plot. The longitude (west)-Ls cross sections for Wave 1, 2, and 3 are displayed in (b), (c) and (d). They use the same color bar next to (b).

with a period of ∼5 weeks and an amplitude of ∼15° in longitude. The locations of southward (negative) eddy meridional wind for Wave 3 appear to coincide with low topography.

[30] Since each data point in Figure 9a represents the mean of all the measurements collected near a grid point during a week, contributions from shorter period (<7 sols) traveling waves are expected to be averaged out. *Banfield et al.* [2003] show that the 2PM–2AM sampling strategy of MGS can result in certain thermal tides and stationary waves being aliased to appear identical. Discrimination between different modes is difficult since most of our measurements are collected in the early afternoon (we did not record the exact local time for each vector). On the basis of discussions by *Banfield et al.* [2003], what MGS sees as Wave 1 is probably dominated by stationary Wave 1 with contributions from several nonmigrating semidiurnal tides, what MGS sees as Wave 2 at high latitudes is probably dominated by stationary Wave 2. *Banfield et al.* [2003] find only small amplitude for Wave 3, but it is likely that Wave 3 is confined to the lower atmosphere where TES retrieval is not accurate enough (D. Banfield, personal communication, 2003).

5.2. Eddy Momentum Flux and Eddy Kinetic Energy

[31] Figure 10 shows polar stereographic maps (62°N–78°N) of eddy momentum flux $\overline{u'v'}$ and eddy kinetic energy $(u'^2 + v'^2)/2$ for four 2-week periods that have good spatial coverage of cloud-tracked winds, where $u' = u - \bar{u}$, $v' = v - \bar{v}$. Again, we assumed that the measured winds were at the same height. Positive value of eddy momentum flux (red in the left panels of Figure 10) indicates poleward transport of eastward momentum or equatorward transport of westward momentum by the wave. Negative value (blue in the left panels of Figure 10) indicates poleward transport of westward momentum or equatorward transport of eastward

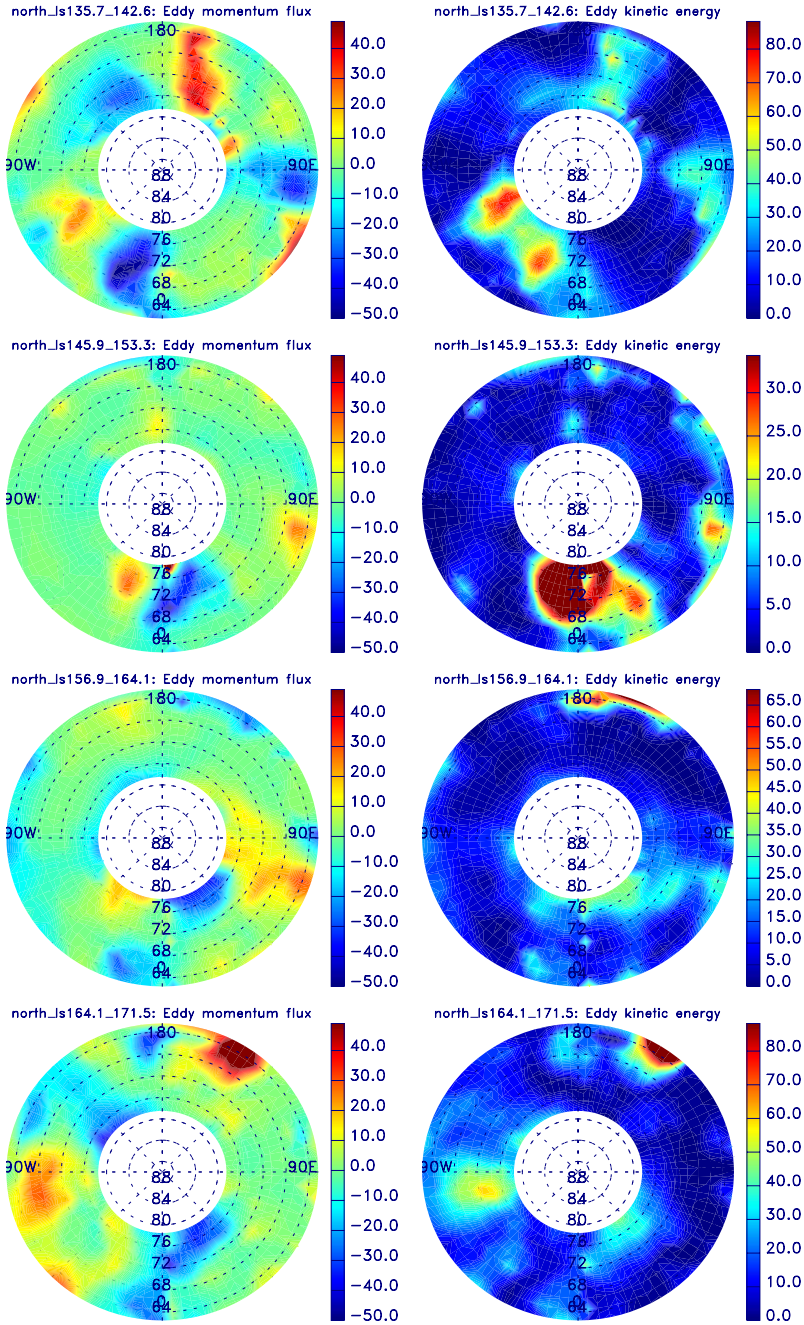

Figure 10. Eddy momentum flux ($u'v'$, m^2/s^2, left panels) and eddy kinetic energy ($0.5(u'^2 + v'^2)$, m^2/s^2, right panels) derived from cloud-tracked winds. L_s is indicated above each panel. Longitudes and latitudes are indicated in each panel.

momentum by the wave. The average eddy momentum fluxes for the four periods are slightly negative (>−2 m^2/s^2), but the spatial distribution for each period shows large-scale waves with large amplitudes (up to 40 m^2/s^2). Depending on the latitude and time, either Wave 2 or Wave 3 appears to dominate the spatial distribution of eddy momentum flux. The wave amplitudes for L_s 135.7°–142.6° and L_s 164.1°–171.5° appear larger than those for Ls 145.9°–153.3° and L_s 156.9°–164.1°. The detailed distribution also changes from one period to another. For example, positive eddy momentum flux occurs in the 135°E–180°E sector during L_s 135.7°–142.6° and L_s 164.1°–171.5°, but not during L_s 145.9°–153.3° and L_s 156.9°–164.1°. However, there appears to be a persistent positive-negative-positive wave pattern with respect to longitude in the 60°W–0°–90°E sector (northeast of Tharsis), though the wave pattern shifts slightly in longitudes for different periods. Referring to Figure 3, we see that the shift appears to be associated with the shift in the position of the cyclonic gyre in the 90°W–0°–30°E sector. The eddy kinetic energy maps for the four periods are shown in the right columns of Figure 10. Regions of large eddy kinetic energy correspond to regions of large positive or negative eddy momentum flux. Although different periods have different activity centers, all the centers

occur in the 90°W–0°–60°E (Acidalia), 135°E–180°E (Arcadia) sectors, and around 90°E (Utopia). *Hollingsworth et al.* [1996] simulated strong eddy activities in these regions using NASA Ames GCM, and pointed out that they are controlled by topography.

6. Summary

[32] We measured cloud-tracked winds for the first MGS mapping year using MOC wide-angle global map swaths. Due to the limitations of the data, our measurements are concentrated in the north polar region during L_s 135°–195° and L_s 20°–55°, and in the south polar region during L_s 337°–10°. We do not have direct information about cloud height. *Smith* [2002] estimated the altitude of the water vapor condensation level to be in the range 5–10 km during the season of our north polar measurements. At this altitude, the wind speeds computed by the NASA Ames GCM generally agree with our measurements. For the south polar region, we tracked dust clouds using red images. The measured winds are much weaker than the GCM simulated winds at the water vapor condensation level (∼10 km). This suggests that the height of the observed dust clouds was lower than 10 km since GCM predicts slower wind speed at lower altitude. The observed mean zonal wind increases from late summer to early fall in both hemispheres, and decreases in the spring in the north polar region. In the north, the zonal wind increase from late summer to early fall appears larger at the higher latitudes. The curvature of the absolute vorticity within 60°N–70°N indicates the possibility of barotropic instability during L_s 135°–195°. A cyclonic gyre in the 90°W–0°–30°E sector at northern high latitudes is observed. It is associated with large eddy momentum fluxes and eddy kinetic energy, and implies poleward transport of water vapor at the level of observed clouds. The longitudinal distribution of meridional winds at 70°N indicates the presence of large-scale waves during L_s 135°–171°. The Wave 2 and 3 components appear to oscillate in phase and amplitude. Due to the sampling strategy of MGS, waves derived from our data could contain stationary waves and certain modes of thermal tides. Wave 1 and 2 are probably dominated by stationary waves. Wave 3 is probably confined in the lower atmosphere. Large amplitude waves are also observed in the eddy momentum flux field. There appear to be a positive-negative-positive pattern northeast of Tharsis. Consistent with GCM simulations, strong eddy activities exist in northern Acidalia, Arcadia and Utopia. These locations also correspond to the southward meridional winds of Wave 3. Our measured winds are stronger than the gradient winds at the water vapor condensation level derived from TES. However, uncertainties in our measurements (velocity, height), TES retrieval, and GCM simulations greatly complicate comparisons between them. Future work is needed to better understand the results presented here and to use them to constrain atmospheric models.

[33] **Acknowledgments.** We thank Michael D. Smith for providing us gradient winds in digital form. We thank Don Banfield and an anonymous reviewer for comments about improving this paper.

References

Banfield, D., B. J. Conrath, M. D. Smith, P. R. Christensen, and R. J. Wilson, Forced waves in the Martian atmosphere from MGS TES nadir data, *Icarus*, *161*, 319–345, 2003.

Barnes, J. R., J. B. Pollack, R. M. Haberle, C. B. Leovy, R. W. Zurek, H. Lee, and J. Schaeffer, Mars atmospheric dynamics as simulated by the NASA Ames General Circulation Model: 2. Transient baroclinic eddies, *J. Geophys. Res.*, *98*, 3125–3148, 1993.

Haberle, R. M., J. B. Pollack, J. R. Barnes, R. W. Zurek, C. B. Leovy, J. R. Murphy, H. Lee, and J. Schaeffer, Mars atmospheric dynamics as simulated by the NASA Ames general circulation model: 1. The zonal-mean circulation, *J. Geophys. Res.*, *98*, 3093–3123, 1993.

Held, I. M., The general circulation of the atmosphere, 2000 program of study in geophysical fluid dynamics, *Woods Hole Oceanogr. Inst. Tech. Rep. WHOI-2001-03*, Woods Hole, Mass., 2001.

Hess, S., R. Henry, C. Leovy, J. Ryan, and J. Tillman, Meteorological results from the surface of Mars: Viking 1 and 2, *J. Geophys. Res.*, *82*, 4559–4574, 1977.

Hollingsworth, J. L., R. M Haberle, J. R. Barnes, A. F. C. Bridger, J. B. Pollack, H. Lee, and J. Schaeffer, Orographic control of storms zones on Mars, *Nature*, *380*, 413–416, 1996.

Kahn, R., Some observational constraints on the global-scale wind systems of Mars, *J. Geophys. Res.*, *88*, 10,189–10,209, 1983.

Kahn, R., and P. Gierasch, Long cloud observations on Mars and implications for boundary layer characteristics over slopes, *J. Geophys. Res.*, *87*, 867–880, 1982.

Malin, M. C., and K. S. Edgett, Mars Global Surveyor Mars Orbiter Camera: Interplanetary cruise through primary mission, *J. Geophys. Res.*, *106*, 23,429–23,570, 2001.

Mischna, M. A., J. F. Bell III, P. B. James, and D. Crisp, Synoptic measurements of Martian winds using the Hubble Space Telescope, *Geophys. Res. Lett.*, *25*, 611–614, 1998.

Salby, M. L., *Fundamentals of Atmospheric Physics*, pp. 517–523, Academic, San Diego, Calif., 1996.

Smith, M. D., The annual cycle of water vapor on Mars as observed by the Thermal Emission Spectrometer, *J. Geophys.*, 107, 5115, doi:10.1029/2001JE001522, 2002.

Smith, M. D., J. C. Pearl, B. J. Conrath, and P. R. Christensen, Thermal Emission Spectrometer results: Mars atmospheric thermal structure and aerosol distribution, *J. Geophys. Res.*, *106*, 23,929–23,945, 2001.

Sullivan, R., R. Greeley, M. Kraft, G. Wilson, M. Golombek, K. Herkenhoff, J. Murphy, and P. Smith, Results of the imager for Mars Pathfinder windsock experiment, *J. Geophys. Res.*, *105*, 24,547–24,562, 2000.

Wang, H., and A.P. Ingersoll, Martian clouds observed by Mars Global Surveyor Mars Orbiter Camera, *J. Geophys.*, *107*, 5078, doi:10.1029/2001JE001815, 2002.

A. P. Ingersoll and H. Wang, Division of Geological and Planetary Sciences, California Institute of Technology, 150-21, Pasadena, CA 91125, USA. (hqw@gps.caltech.edu)